

Quantum Simulation of the Schwinger Model: Final Term Project Report

Abhijeet Bhatta, Chayanka Kakati
Course: Quantum Field Theory on a Quantum Computer
Center for High Energy Physics, IISC

December 1, 2025

Abstract

We study the Schwinger Model in detail and discuss how to simulate it on a Quantum Computer. We also show phenomena like particle production and string breaking on Qiskit.

Contents

| | | | | | |
|----------|--|----------|------------|--|-----------|
| 1 | Introduction | 2 | 6.2 | Trotterized Evolution Loop | 8 |
| 2 | From Continuum Dirac Theory to the Lattice | 2 | 6.3 | Measurement and Observables | 8 |
| 2.1 | Staggered Lattice Hamiltonian and decoupling into two chains | 2 | 7 | Results: Pair Production and Vacuum Decay | 8 |
| 2.2 | Kogut–Susskind single-component mapping | 2 | 7.1 | Dynamics of Charge Density | 9 |
| 2.3 | Gauge Invariance and the Kogut–Susskind Hamiltonian | 2 | 7.2 | Time Evolution of Particle Number Density | 9 |
| 3 | Encoding the Hamiltonian for Quantum Simulation | 3 | 8 | Benchmarking Trotter Dynamics against Exact Diagonalization | 10 |
| 3.1 | Jordan–Wigner mapping | 3 | 8.1 | Exact Diagonalization Setup | 10 |
| 3.2 | Gauge Fixing and Elimination of Fields | 3 | 8.2 | Comparison Results | 10 |
| 3.3 | Final qubit Hamiltonian | 4 | 8.3 | Vacuum Structure and Adiabatic Connectivity | 11 |
| 4 | Ground State and Particle Interpretation | 4 | 9 | Observation of String Breaking and Charge Screening | 12 |
| 4.1 | Particle-Hole Transformation and Vacuum | 4 | 9.1 | Setup: Initializing a Flux String | 12 |
| 5 | Time Evolution and Trotterization | 5 | 9.2 | Dynamics of Charge Screening | 12 |
| 5.1 | The First-Order Trotter Decomposition | 5 | 9.3 | Collapse of the Electric Field | 13 |
| 5.2 | Circuit Implementation | 6 | 10 | Pair production vs particle mass | 13 |
| 6 | Simulation Implementation and Results | 6 | 10.1 | Pair production in Vacuum vs Mass | 14 |
| 6.1 | Ground State and String Initialization | 7 | 10.2 | String Breaking vs Mass | 14 |
| | | 7 | 11 | Dynamical Phase Transition and the θ-Vacuum | 14 |
| | | 7 | 11.1 | Dynamical Sweep Protocol | 15 |
| | | 7 | 11.2 | Results: The Chiral Condensate | 15 |

1 Introduction

Quantum simulation offers a structurally different approach compared to traditional methods in Perturbative Quantum Field Theory. Instead of relying on a series expansion, the evolution operator is constructed directly as a product of unitary gates. In this setting,

$$\hat{U}(t) \approx \prod_k e^{-iH_k \Delta t}, \quad (1)$$

where the Hamiltonian has been decomposed into simple components H_k whose exponentials can be implemented on quantum hardware. This Trotterized evolution remains unitary at every step, guaranteeing probability conservation by construction. The simulation therefore mirrors the physical dynamics more faithfully than perturbative methods and provides a natural platform for studying real-time processes that are challenging for classical computation.

2 From Continuum Dirac Theory to the Lattice

We begin with the Dirac Hamiltonian density in $(1+1)$ dimensions,

$$\mathcal{H} = -i\bar{\psi}\gamma^i\partial_i\psi + m\bar{\psi}\psi, \quad (2)$$

where $\psi(t, x)$ is a two-component Dirac spinor, $\bar{\psi} = \psi^\dagger\gamma^0$, m is the fermion mass, and γ^μ are the Dirac matrices. In the Dirac representation for $(1+1)$ dimensions,

$$\gamma^0 = \sigma^3, \quad \gamma^1 = i\sigma^2, \quad (3)$$

so the spinor may be written as

$$\psi = \begin{pmatrix} \psi_e \\ \psi_o \end{pmatrix}, \quad (4)$$

which correspond to the two fermionic degrees of freedom per lattice site.

Lattice Discretization

To place the theory on a spatial lattice with spacing a , we use the symmetric difference to discretize the spatial derivative,

$$\partial_1\psi(x) \longrightarrow \frac{\psi(n+1) - \psi(n-1)}{2a}, \quad (5)$$

and rescale the fields so that the lattice fermions have canonical anticommutation relations,

$$\psi_{e/o}(x) \longrightarrow \frac{1}{\sqrt{a}}\psi_{e/o}(n). \quad (6)$$

Each lattice site n carries two fermionic modes, $\psi_e(n)$ and $\psi_o(n)$, which originate from the two components of the continuum Dirac spinor. How they couple to each other will only come to light if we look at the structure of that lattice hamiltonian.

2.1 Staggered Lattice Hamiltonian and decoupling into two chains

The discretized fermion Hamiltonian (spatial lattice spacing a) may be written in the form used throughout this work as

$$H_f = \frac{i}{2a} \sum_n \left[\psi_e^\dagger(n)\psi_o(n+1) + \psi_o^\dagger(n)\psi_e(n+1) - \text{h.c.} \right] + m \sum_n \left[\psi_e^\dagger(n)\psi_e(n) - \psi_o^\dagger(n)\psi_o(n) \right]. \quad (7)$$

Two immediate features are clear from (refer to ψ_e as even and ψ_o as odd) (7):

1. The kinetic term couples the even component on site n , only to the odd component on the neighbouring site $n + 1$ (and vice versa). There is no direct hopping between $\psi_e(n)$ and $\psi_e(n \pm 1)$, nor between $\psi_o(n)$ and $\psi_o(n \pm 1)$.
2. The mass term is strictly on-site meaning it couples the even and odd components to itself on that site.

If we separate the fields into these two different sets

$$(\psi_e(n), \psi_o(n+1)) \quad \text{and} \quad (\psi_o(n), \psi_e(n+1))$$

we see that these two different sets of fields are completely decoupled from each other but follow the exact same dynamics in their own set (can be verified by deriving the equation of motion). This is the key idea to the **Kogut–Susskind Mapping**.

2.2 Kogut–Susskind single-component mapping

The decoupling observed above allows us to reinterpret the two Dirac components $\psi_e(n)$ and $\psi_o(n)$ as values of a *single* lattice field living on alternating sites. Concretely, the Kogut–Susskind (KS) staggered fermion field is defined as

$$\varphi(n) = \begin{cases} \psi_e(n), & n \text{ even}, \\ \psi_o(n), & n \text{ odd}. \end{cases} \quad (8)$$

In terms of $\varphi(n)$, the fermionic Hamiltonian takes the familiar KS form:

$$H_{\text{KS}} = \frac{i}{2a} \sum_n \left[\varphi^\dagger(n) \varphi(n+a) - \varphi^\dagger(n+a) \varphi(n) \right] + m \sum_n (-1)^{n/a} \varphi^\dagger(n) \varphi(n). \quad (9)$$

The staggering factor $(-1)^{n/a}$ encodes the original mass splitting between the even and odd components.

2.3 Gauge Invariance and the Kogut–Susskind Hamiltonian

To preserve local $U(1)$ gauge invariance on the lattice, we introduce a unitary *gauge link operator* $U(x)$ on each bond. Physically, this operator acts as a parallel transporter connecting adjacent sites, approximated for small lattice spacing as the exponential of the gauge potential:

$$U(x) \simeq e^{i a g A(x)}, \quad 0 \leq a g A(x) < 2\pi. \quad (10)$$

This promotes the fermion hopping term to the gauge-covariant finite difference $\varphi^\dagger(x) U(x) \varphi(x+a)$, ensuring the Hamiltonian remains invariant under local transformations.

The dynamical gauge degrees of freedom contribute the electric field energy density $\mathcal{H}_{\text{gauge}} = \frac{1}{2} E^2$, where the lattice electric field $E(x)$ is the conjugate variable to the link $U(x)$. Combining the covariant hopping, the staggered mass, and the electric energy yields the full Kogut–Susskind Hamiltonian:

$$H_{\text{KS}}^{1+1} = \frac{i}{2a} \sum_x \left[\varphi^\dagger(x) U(x) \varphi(x+a) - \text{h.c.} \right] + m \sum_x (-1)^{x/a} \varphi^\dagger(x) \varphi(x) + \frac{g^2 a}{2} \sum_x E(x)^2. \quad (11)$$

3 Encoding the Hamiltonian for Quantum Simulation

The lattice Hamiltonian derived above is expressed in terms of staggered fermion operators $\varphi(n)$ and $\varphi^\dagger(n)$, which satisfy the canonical anti-commutation relations

$$\{\varphi(n), \varphi^\dagger(m)\} = \delta_{nm}, \quad \{\varphi(n), \varphi(m)\} = 0. \quad (12)$$

Quantum hardware, however, manipulates qubits. The corresponding operators are Pauli matrices $\{X, Y, Z\}$ acting on tensor-product Hilbert spaces, with the property that operators on distinct sites commute. This contrasts sharply with fermionic operators, whose non-local anti-commutation structure prevents a direct identification with qubit degrees of freedom.

$$\{\varphi, \varphi^\dagger\} \longrightarrow \{X, Y, Z\}, \quad (\text{non-local Jordan--Wigner map}). \quad (13)$$

This mapping replaces the anti-commuting lattice fields with Pauli operators that can be natively implemented on current quantum devices. The resulting Hamiltonian becomes a sum of tensor products of Pauli matrices, suitable for gate-based quantum simulation.

3.1 Jordan–Wigner mapping

The Jordan Wigner Transformation exactly does this job of going from fermionic degrees of freedom to spin 1/2 Paulis:

$$\chi_n = \left(\prod_{l < n} \sigma_l^z \right) \sigma_n^-, \quad \chi_n^\dagger = \left(\prod_{l < n} \sigma_l^z \right) \sigma_n^+, \quad (14)$$

with $\sigma_n^\pm = \frac{1}{2}(\sigma_n^x \pm i\sigma_n^y)$.

Because the Jordan–Wigner strings extend over all sites $l < n$, *boundary conditions* play a crucial role. In particular, periodic boundary conditions would produce terms such as $\varphi_N^\dagger \varphi_1$, whose Jordan–Wigner image contains an extensive string of N Pauli-Z operators. Such operators are highly non-local and render the Hamiltonian inefficient for quantum simulation.

For this reason, throughout this work we impose **open boundary conditions**. This yields a qubit Hamiltonian composed only of local Pauli operators (upto nearest neighbour), suitable for gate-based implementation.

3.2 Gauge Fixing and Elimination of Fields

In 1+1D with open boundary conditions, we can fully eliminate the gauge degrees of freedom. By exploiting the local $U(1)$ gauge symmetry $\varphi_n \mapsto e^{i\alpha_n} \varphi_n$, we can choose the phases $\{\alpha_n\}$ such that every link variable becomes trivial:

$$U_n \rightarrow 1 \quad \forall n.$$

The remaining constraint is Gauss's law, which determines the electric field from the static charge distribution. In terms of the staggered fermions, the law reads $E_n - E_{n-1} = \rho_n$, with charge density $\rho_n = \chi_n^\dagger \chi_n - \frac{1 - (-1)^n}{2}$. Imposing the open boundary condition $E_{-1} = 0$, we solve this explicitly:

$$E_n = \sum_{i=0}^n \rho_i = \sum_{i=0}^n \left(\chi_i^\dagger \chi_i - \frac{1 - (-1)^i}{2} \right). \quad (15)$$

Substituting this result into the electric energy term $H_E \propto \sum E_n^2$ removes all gauge field operators, resulting in a theory of fermions with long-range interactions.

3.3 Final qubit Hamiltonian

We now combine the results of gauge fixing, Gauss's law, and the Jordan–Wigner mapping $\chi_n^\dagger \chi_n \mapsto \frac{1+\sigma_n^z}{2}$ (convention chosen so that occupied sites correspond to $\sigma^z = +1$).

Collecting all pieces, the final qubit Hamiltonian used for simulation is

$$\boxed{H_{\text{qubit}} = \frac{1}{4a} \sum_n (\sigma_n^x \sigma_{n+1}^x + \sigma_n^y \sigma_{n+1}^y) + \frac{m}{2} \sum_n (-1)^n \sigma_n^z + \frac{g^2 a}{2} \sum_n \left[\sum_{i=0}^n \frac{\sigma_i^z + (-1)^i}{2} \right]^2.} \quad (16)$$

- Open boundary conditions were essential to both gauge fixing (setting $U_n = 1$) and to obtaining the explicit solution (15). Periodic boundaries would reintroduce the Gauge Field and non-trivial Jordan–Wigner strings.

4 Ground State and Particle Interpretation

To interpret simulation results, we must map the staggered lattice sites to physical particles. The fermionic mass term $m \sum_n [\psi_e^\dagger \psi_e - \psi_o^\dagger \psi_o]$ dictates that in the heavy-mass ground state $|\Omega\rangle$:

- **Even sites (n even):** Host electrons (mass $+m$) and should be *empty* ($\psi^\dagger \psi = 0$).
- **Odd sites (n odd):** Host positrons (mass $-m$) and should be *filled* ($\psi^\dagger \psi = 1$) to fill the Dirac sea.

4.1 Particle-Hole Transformation and Vacuum

To rigorously define particle content, we employ a particle-hole transformation. We define physical annihilation operators c_n such that $c_n |\Omega\rangle = 0$. This requires $c_n = \psi_n$ for even sites and $c_n = \psi_n^\dagger$ for odd sites. The resulting physical particle number operator is:

$$\hat{N}_n = c_n^\dagger c_n = \begin{cases} \psi_n^\dagger \psi_n & n \text{ even (electrons)}, \\ 1 - \psi_n^\dagger \psi_n & n \text{ odd (positrons)}. \end{cases} \quad (17)$$

Mapping this to qubits via our convention yields $\hat{N}_n^{\text{qubit}} |\Omega\rangle = 0$ for the state $|\mathbf{1010}\dots\rangle$. This state serves as the ideal initial vacuum $|\psi(0)\rangle$ for our simulation, as it is adiabatically connected to the interacting vacuum and can be prepared with $O(1)$ depth by applying Pauli-X gates to all even-indexed qubits.

5 Time Evolution and Trotterization

Having derived the qubit Hamiltonian H in Eq. (22) and identified the initial vacuum state $|\mathbf{1010}\dots\rangle$ in Section 4, we now turn to simulating the time evolution of the system, governed by the unitary operator $U(t) = e^{-iHt}$.

Since the terms in the Hamiltonian do not commute (specifically, the kinetic term $H_K \sim \sum \sigma^+ \sigma^-$ does not commute with the electric field term $H_E \sim \sum \sigma_i^z \sigma_j^z$), we cannot simply exponentiate them individually. Instead, we employ the Suzuki-Trotter decomposition to approximate the time evolution operator for a small time step Δt .

5.1 The First-Order Trotter Decomposition

We decompose the total Hamiltonian from Eq. (22) into three distinct parts based on their Pauli structures:

$$H = H_{ZZ} + H_Z + H_K \quad (18)$$

Where:

- H_{ZZ} contains all terms proportional to $\sigma_i^z \sigma_j^z$ (arising from the E^2 term).
- H_Z contains all terms proportional to σ_i^z (arising from the mass term and the linear parts of the E^2 term).

For the mass term $\frac{m}{2} \sum_n (-1)^n \sigma_n^z$: We get a H_z^{mass} contribution.

The more difficult term is $\frac{g^2 a}{2} \sum_n \left[\sum_{i=0}^n \frac{\sigma_i^z + (-1)^i}{2} \right]^2$ for which we will get both H_{zz} and H_z contributions. Decomposing the entire sum we evaluate:

$$H_{ZZ} = \sum_{m < \ell < N} \frac{g^2 a}{4} (N - 1 - \ell) \sigma_m^z \sigma_\ell^z, \quad H_Z^{electric} = \sum_{m=0}^{N-1} \frac{g^2 a}{4} [w_m^{(1)} + w_m^{(2)} + w_m^{(3)}] \sigma_m^z$$

$$A(K) = \begin{cases} K/2, & K \text{ even}, \\ -(K+1)/2, & K \text{ odd}, \end{cases}$$

$$w_m^{(1)} = (N-1-m)(-1)^m, \quad w_m^{(2)} = (-1)^{N-1} A(N-2-m), \quad w_m^{(3)} = \frac{N-1-m}{2} (1-(-1)^m).$$

We get the following weighted coefficients for H_Z term and we also see a H_{zz} term will all possible pairs.

- H_K is the kinetic "hopping" term, proportional to $x \sum (\sigma_n^+ \sigma_{n+1}^- + h.c.)$, which can be rewritten in terms of XX and YY interactions:
 $\frac{1}{4a} \sum (\sigma_n^x \sigma_{n+1}^x + \sigma_n^y \sigma_{n+1}^y)$.

The first-order Trotter approximation for one time step is given by:

$$e^{-iH\Delta t} \approx e^{-iH_{ZZ}\Delta t} e^{-iH_Z\Delta t} e^{-iH_K\Delta t} + O(\Delta t^2). \quad (19)$$

To simulate evolution up to a total time T , we repeat this single Trotter step N_t times, where $T = N_t \Delta t$.

5.2 Circuit Implementation

Each exponential term in the Trotter decomposition corresponds to a specific set of quantum gates.

1. **Z and ZZ Rotations:** The terms $e^{-i\theta\sigma^z}$ correspond to single-qubit $R_z(2\theta)$ rotation gates. The interaction terms $e^{-i\theta\sigma_i^z\sigma_j^z}$ are implemented using a CNOT-Rz-CNOT sequence between qubits i and j . Since all Z and ZZ terms commute with each other, their ordering within this block does not matter.

2. **$XX + YY$ (Hopping) Rotations:** The kinetic term $e^{-i\frac{x\Delta t}{2}(\sigma_n^x\sigma_{n+1}^x + \sigma_n^y\sigma_{n+1}^y)}$ requires a more complex gate decomposition as shown in Figure 2.

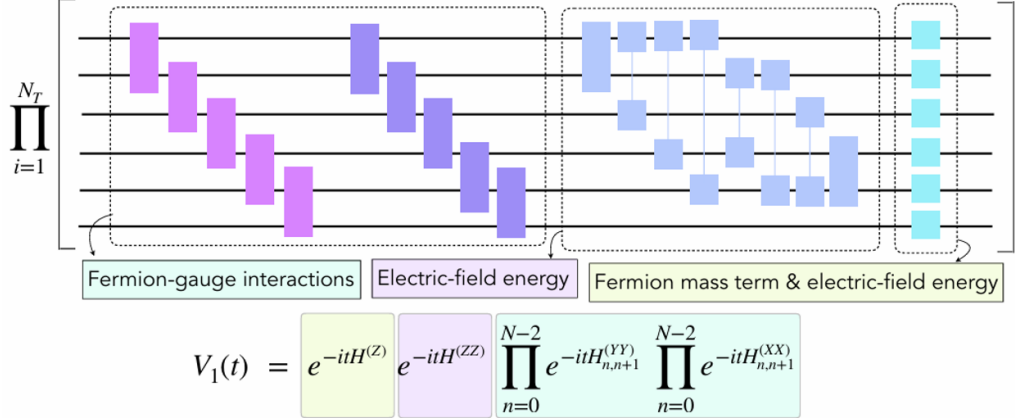


Figure 1: Complete Trotter step circuit

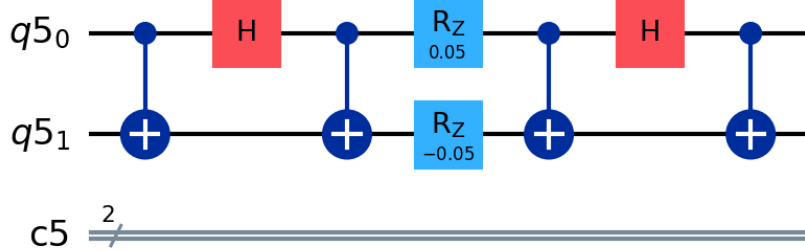


Figure 2: Quantum circuit decomposition for the kinetic (hopping) term

6 Simulation Implementation and Results

We implemented the time evolution of the Schwinger model using IBM’s Qiskit framework. The simulation proceeds in three distinct stages: state preparation, Trotterized time evolution, and measurement of physical observables.

6.1 Ground State and String Initialization

The simulation begins by preparing the system in a specific initial state $|\psi(0)\rangle$. As derived in Section 4, the heavy-mass vacuum (the state with zero physical particles) corresponds to the product state:

$$|\Omega\rangle = |101010\dots\rangle. \quad (20)$$

In Qiskit, qubits are initialized to $|0\rangle$. To prepare $|\Omega\rangle$, we apply Pauli- X gates to all even-indexed qubits ($n = 0, 2, \dots$), as shown in the code snippet.

To study dynamical phenomena such as *string breaking*, we must excite the vacuum. We introduce an external static quark-antiquark pair by flipping the spins at the boundaries of the lattice:

- At $n = 0$ (even), we apply an X gate. This transforms $|1\rangle \rightarrow |0\rangle$, creating an electron ($Q = +1$).
- At $n = N - 1$ (odd), we apply an X gate. This transforms $|0\rangle \rightarrow |1\rangle$, creating a positron ($Q = -1$).

This establishes a state $|\psi(0)\rangle = |0010\dots11\rangle$ containing a flux string (electric field) stretching across the lattice between the static charges. The subsequent dynamics will investigate the stability of this string.

6.2 Trotterized Evolution Loop

The time evolution $U(t) = e^{-iHt}$ is approximated using the first-order Trotter-Suzuki decomposition. The total simulation time $T = 10$ is divided into $N_{\text{steps}} = 50$ steps, with $\Delta t = 0.2$. In every step, the circuit implements the three non-commuting parts of the Hamiltonian sequentially:

1. **Kinetic Term (H_{XX+YY}):** We implement nearest-neighbor hopping using the gate sequence:

$$e^{-i\theta(XX+YY)} \equiv \text{CNOT} \cdot R_Z(\theta) \cdot R_Z(-\theta) \cdot \text{CNOT}, \quad (21)$$
flanked by basis change gates (Hadamard and CNOTs) to diagonalize the interactions.
2. **Mass Term (H_Z):** This is implemented via single-qubit R_Z rotations. The rotation angle for site n is determined by the staggered mass parameter $M(-1)^n \Delta t$.
3. **Electric Field Term ($H_{ZZ} + H_Z$):** The long-range Coulomb interaction derived in Eq. (22) leads to all-to-all ZZ interactions. In our code, we iterate through all pairs (k, l) and apply R_{ZZ} gates with weights proportional to the distance $N - 1 - l$. This non-local connectivity is the computational bottleneck of the 1D Schwinger model simulation.

6.3 Measurement and Observables

At each time step, the system is measured in the computational basis. We performed $N_{\text{shots}} = 10,000$ shots to construct the probability distribution of bitstrings. From these bitstrings, we reconstruct the physical observables:

- **Charge Density ρ_n :** We map the measured bits $b_n \in \{0, 1\}$ to physical charges. If n is even, a '0' bit implies $Q = +1$. If n is odd, a '1' bit implies $Q = -1$ (in units of the electron charge).
- **Electric Field E_n :** Using the discrete Gauss's law derived in Eq. (21), the electric field on link n is computed as the cumulative sum of charges to its left:

$$E_n = \sum_{i=0}^n \rho_i. \quad (22)$$

- **Particle Number Density:** We compute the total number of particle-antiparticle pairs generated from the vacuum to track the energy conversion from the electric field to mass.

7 Results: Pair Production and Vacuum Decay

A hallmark prediction of the Schwinger model (and QED in strong fields) is the instability of the vacuum in the presence of an electric field. In $1 + 1$ dimensions, even a small external field (or quantum fluctuations in the massless limit) can spontaneously generate electron-positron pairs, screening the field and leading to oscillatory dynamics in particle density.

To observe this phenomenon, we initialize the system in the bare vacuum state $|\Omega\rangle = |1010\dots\rangle$, which corresponds to zero charge density everywhere ($\rho_n(0) = 0$). We then evolve this state under the full Hamiltonian with parameters $m = 0.083$, $g = 1.29$, and measure the local charge density $\langle \rho_n(t) \rangle$ as a function of time.

7.1 Dynamics of Charge Density

The evolution of the local charge density for an $N = 4$ site lattice is shown in Figure 3.

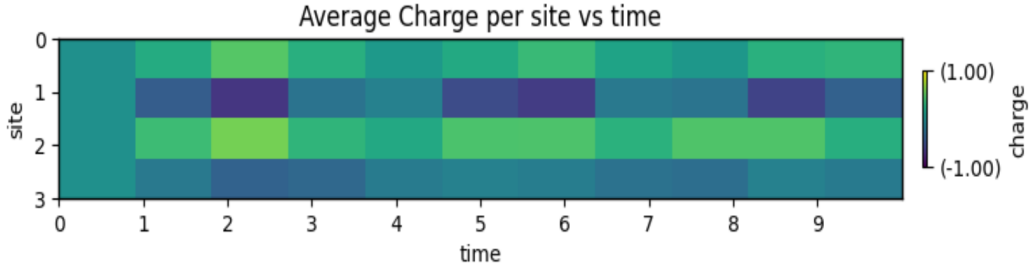


Figure 3: Time evolution of the average charge density $\langle \rho_n(t) \rangle$ for an $N = 4$ lattice site system, simulated using 10 Trotter steps with $T_{max} = 10$. The color scale indicates the local charge, where yellow (+1) corresponds to an electron and blue (-1) to a positron. The system initializes in the neutral vacuum (green, charge 0) and exhibits spontaneous fluctuations into charged states.

The heat map reveals the following dynamical features:

- **Initial State ($t = 0$):** The system starts with charge density close to zero at all sites (represented by the uniform teal color), consistent with the prepared state $|\Omega\rangle$.
- **Pair Creation ($t > 0$):** As time evolves, we observe the emergence of positive charge density (yellow/green) on even sites and negative charge density (purple/blue) on odd sites. This signifies the spontaneous creation of $e^- e^+$ pairs from the vacuum energy.
- **Oscillations:** The system does not settle into a steady state but oscillates between the neutral vacuum and states with high particle density. This coherent oscillation is a signature of the finite-size lattice, where created pairs cannot escape to infinity but instead recombine and re-emerge.

These results confirm that our quantum circuit successfully captures the non-perturbative Schwinger mechanism, where the vacuum is not an eigenstate of the full interacting Hamiltonian and decays into particle-antiparticle pairs.

7.2 Time Evolution of Particle Number Density

In addition to local charge distributions, a key global observable is the average particle number density, $\nu(t)$. This quantity tracks the total number of physical excitations (electrons plus positrons) present in the lattice as a function of time.

Based on our particle-hole definition of the number operator in Eq. (23), the total particle number operator is the sum of electrons on even sites and positrons on odd sites. The average density is normalized by the system size N :

$$\hat{\nu} = \frac{1}{N} \sum_{n=0}^{N-1} \hat{N}_n^{\text{qubit}} = \frac{1}{N} \sum_{n=0}^{N-1} \frac{1 + (-1)^n \sigma_n^z}{2}. \quad (23)$$

We computed the expectation value $\nu(t) = \langle \psi(t) | \hat{\nu} | \psi(t) \rangle$ using the measurement counts from the quantum simulation.

The results for an $N = 6$ lattice are shown in Figure 4. The dynamics display characteristic features of the Schwinger model in the unstable vacuum regime:

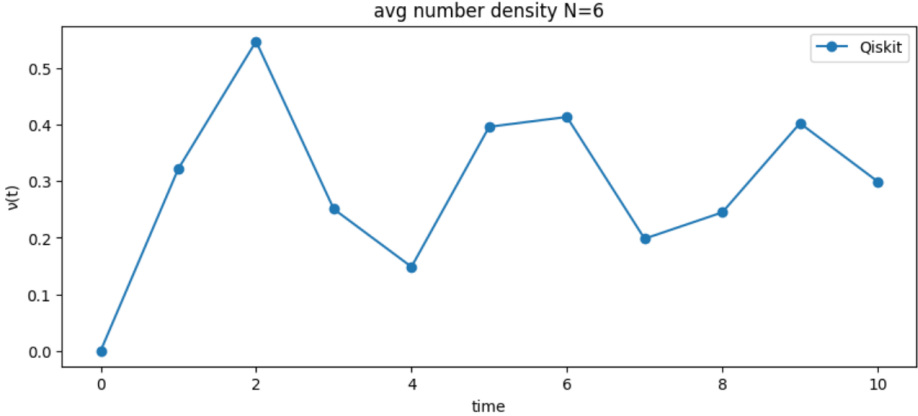


Figure 4: Time evolution of the average particle number density $\nu(t)$ for an $N = 6$ site lattice. The system is initialized in the vacuum state $|\Omega\rangle$ (where $\nu(0) = 0$). The points represent the Trotterized quantum simulation results obtained from Qiskit.

- **Vacuum Instability:** Starting from $\nu(0) = 0$, the density rises rapidly, reaching a local maximum around $t \approx 2$. This confirms the spontaneous creation of particle-antiparticle pairs driven by the vacuum energy.
- **Coherent Oscillations:** Rather than saturating, the density oscillates. This behavior arises because the created pairs, being massive and confined by the 1D Coulomb potential, eventually lose kinetic energy, stop, and recombine. The system undergoes coherent cycles of pair creation and annihilation.

This plot serves as a direct benchmark of the quantum simulation, reproducing the known oscillatory behavior of the order parameter in the Schwinger model.

8 Benchmarking Trotter Dynamics against Exact Diagonalization

To validate the accuracy of our Trotterized quantum simulation, we compare the results of the $N = 6$ qubit simulation against a classical exact diagonalization of the Hamiltonian. The observable of interest is the average particle number density $\nu(t)$, which serves as a global order parameter for vacuum instability and pair production.

8.1 Exact Diagonalization Setup

The exact time evolution is computed by constructing the full Hamiltonian matrix H (dimension $2^6 \times 2^6$) using the parameters $m = 0.083, g = 1.29$. The time evolution of the initial state $|\psi(0)\rangle$ is obtained via the spectral decomposition:

$$|\psi(t)\rangle_{\text{exact}} = \sum_k c_k e^{-iE_k t} |E_k\rangle, \quad (24)$$

where $\{E_k, |E_k\rangle\}$ are the eigenvalues and eigenstates of H , and $c_k = \langle E_k | \psi(0) \rangle$ are the overlap coefficients. The exact particle density is then computed as $\nu_{\text{exact}}(t) = \langle \psi(t) | \hat{\nu} | \psi(t) \rangle$.

8.2 Comparison Results

Figure 5 displays the comparison between the Qiskit Trotter simulation (orange points) and the exact classical result (blue curve) for two different time discretizations.

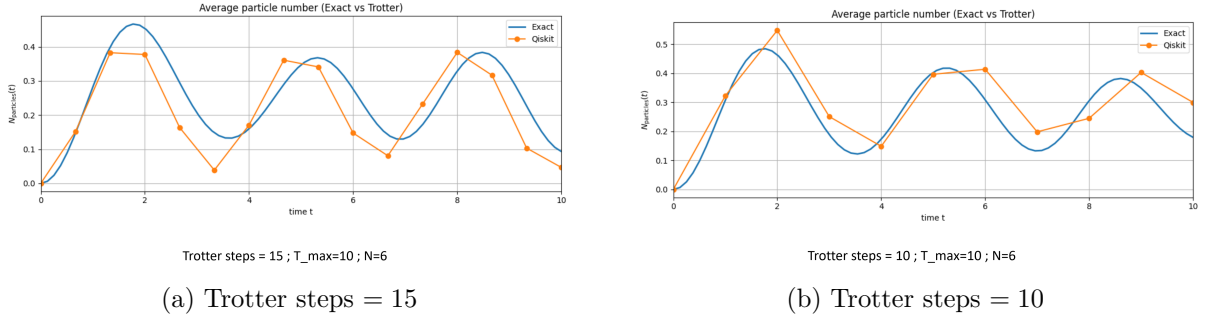


Figure 5: Comparison of particle number density evolution $\nu(t)$ between exact diagonalization (solid blue line) and Trotterized quantum simulation (orange points) for an $N = 6$ lattice. (a) With 15 Trotter steps, the simulation captures the frequency and amplitude of the oscillations with moderate accuracy. (b) With 10 Trotter steps, we observe significant deviations in amplitude and a slight phase shift at later times, indicative of Trotter error.

The plots reveal the impact of the Trotter approximation error, just 5 more steps reducing it significantly.

8.3 Vacuum Structure and Adiabatic Connectivity

Using exact diagonalization, we can probe the structure of the theory's true ground state $|\Omega_{\text{exact}}\rangle$ as a function of the fermion mass m . A crucial metric for our quantum simulation strategy is the fidelity (overlap) between the true interacting ground state and our computational basis initialization state $|\psi_{\text{bare}}\rangle = |1010\dots\rangle$.

Figure 6 plots this overlap, $\mathcal{F}(m) = |\langle \psi_{\text{bare}} | \Omega_{\text{exact}}(m) \rangle|^2$, for an $N = 6$ system with fixed coupling $g^2 = 1.66$.

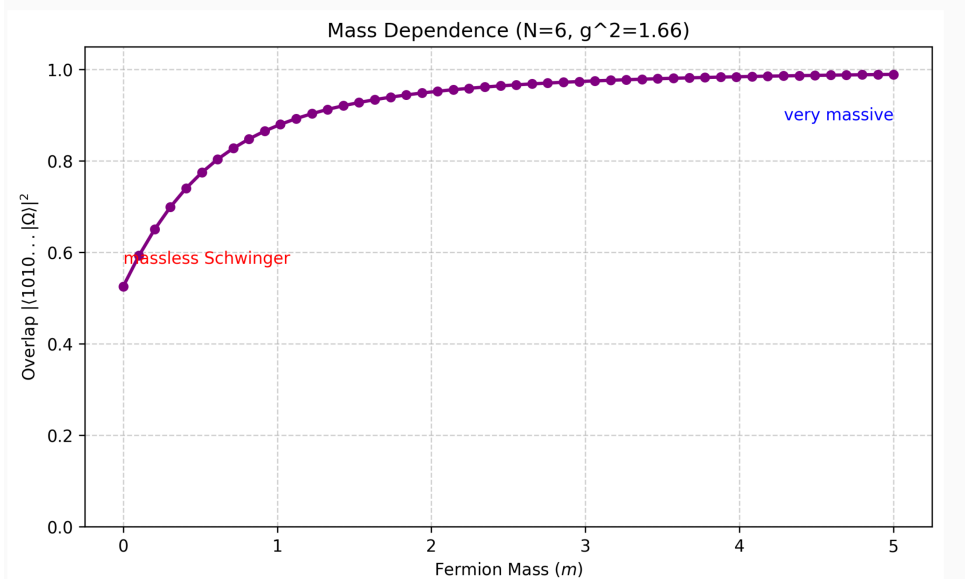


Figure 6: Dependence of the vacuum fidelity on the fermion mass m for $N = 6$ and $g^2 = 1.66$. The plot shows the squared overlap between the bare lattice vacuum $|1010\dots\rangle$ and the exact ground state of the full Hamiltonian. The smooth monotonic increase confirms that the two states are adiabatically connected.

The results illuminate two distinct physical regimes:

- **Massless Limit ($m \rightarrow 0$):** In the massless Schwinger model, the vacuum is a complex

superposition teeming with particle-antiparticle pairs due to strong quantum fluctuations. Consequently, the overlap with the “empty” bare vacuum is relatively low (≈ 0.5). The ground state here is a non-trivial chiral condensate.

- **Heavy Mass Limit ($m \rightarrow \infty$):** As the mass increases, the energy cost of creating particle pairs ($2m$) eventually outweighs the kinetic and electric field gains. The vacuum fluctuations are suppressed, and the system is forced into the lowest energy configuration of the mass term. We observe the overlap converging asymptotically to 1.0, confirming that for heavy fermions, the interacting vacuum is effectively the empty state $|1010\dots\rangle$.

Crucially, the curve is smooth and monotonic. This lack of discontinuity indicates that there is no quantum phase transition separating the massless and massive regimes.

9 Observation of String Breaking and Charge Screening

One of the most profound non-perturbative phenomena in gauge theories is confinement and string breaking. When two static external charges are separated, a flux tube (or string) of the gauge field forms between them. As the separation increases, the energy stored in the string grows linearly. Eventually, it becomes energetically favorable for the vacuum to snap the string by creating a dynamical particle-antiparticle pair, which screens the external charges and reduces the field energy.

9.1 Setup: Initializing a Flux String

To simulate this, we modify our initial state preparation. Instead of the bare vacuum, we prepare a state with a static electron at site $n = 0$ and a static positron at site $n = N - 1$. In our qubit mapping (Convention A), this corresponds to flipping the boundary spins:

$$|\psi(0)\rangle = X_0 X_{N-1} |\Omega\rangle = |0\rangle_0 \otimes |0\rangle_1 \dots |1\rangle_{N-2} \otimes |1\rangle_{N-1}. \quad (25)$$

Physically, this boundary condition forces a non-zero electric field $E = 1$ across the entire bulk of the lattice at $t = 0$, representing a highly excited string state connecting the external charges.

9.2 Dynamics of Charge Screening

We evolve this string state using the same Hamiltonian parameters ($N = 6, m = 0.083, g = 1.29$) and measure the local charge density. Figure 7 visualizes the results.

The heat map shows a clear progression:

1. **Early Time ($t < 2$):** The bulk remains largely neutral (green), sustaining the electric flux between the boundary charges.
2. **String Breaking ($t \approx 3$):** We observe the spontaneous appearance of charge density in the bulk. Specifically, positive charge accumulates near the negative boundary, and negative charge accumulates near the positive boundary.
3. **Screening ($t = 10$):** By the end of the simulation, the most probable state is $|010101\rangle$, which corresponds to a crystal of alternating charges: $e^+e^-e^+e^-e^+e^-$. This new configuration locally neutralizes the electric field, effectively breaking the original long string into smaller, lower-energy dipoles.

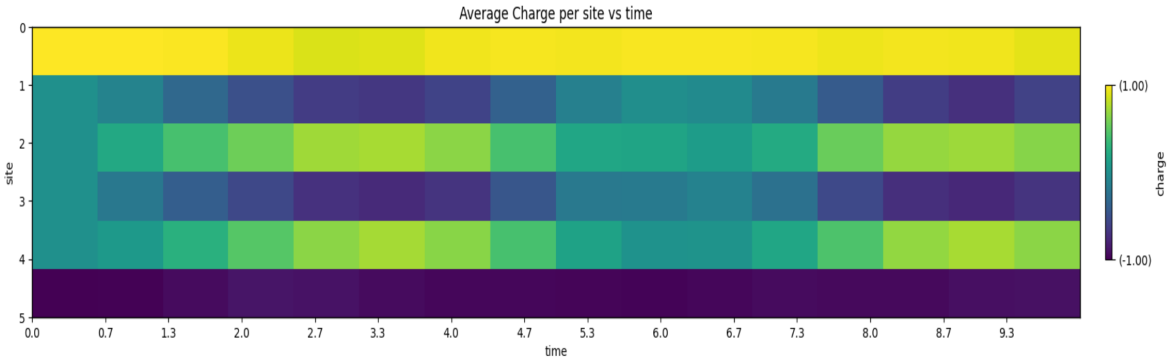


Figure 7: Time evolution of charge density during string breaking for $N = 6$. The system is initialized with static external charges at the boundaries: an electron at $n = 0$ (yellow stripe) and a positron at $n = 5$ (purple stripe). As time evolves, dynamical pairs are created in the bulk (intermediate stripes appearing at $t > 2$)

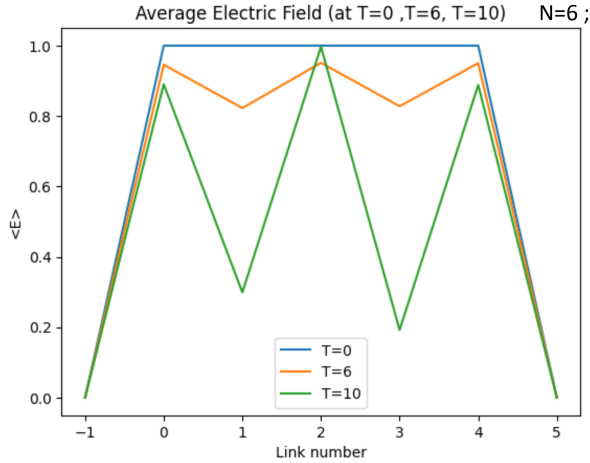


Figure 8: Snapshots of the average electric field profile $\langle E_n \rangle$ across the lattice links. At $t = 0$ (blue line), a uniform field $E = 1$ stretches across the entire lattice, connecting the boundary charges. At $t = 6$ (orange line), the field begins to sag in the middle. By $t = 10$ (green line), the field in the center has collapsed significantly ($\langle E \rangle \approx 0.2$), confirming that the creation of dynamical pairs has screened the external field and broken the string.

9.3 Collapse of the Electric Field

To confirm that the string has indeed broken, we reconstruct the electric field dynamics using Gauss's Law, $E_n = \sum_{i=0}^n \rho_i$. Figure 8 shows the profile of the electric field across the lattice links at three snapshots in time.

Another thing we noticed is that, as we increase the mass parameter in the Hamiltonian, string breaking becomes increasingly more difficult as each pair needs more energy to be produced.

10 Pair production vs particle mass

As we increase the mass of the fermion/anti-fermion i.e. increase the value ' m ' in the Hamiltonian the mass term dominates over the kinetic and the electric field term. Thus the Vacuum state becomes closer to the ground state as mass is increased. This results in reduced tendency of deviating from the vacuum by pair production. It can also be interpreted as the increased mass

makes it difficult for new pairs to be produced as it takes more energy to produce them.

10.1 Pair production in Vacuum vs Mass

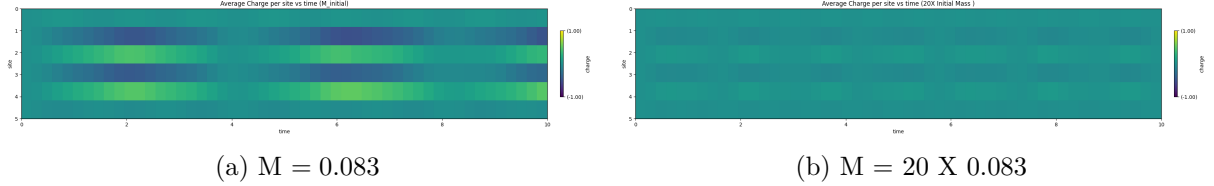


Figure 9: Comparison of average charge for low and high mass regime starting from vacuum. As for all other simulations $M_{initial} = 0.083$ and $g = 1.29$. For figure (b) we use $20.M_{initial}$ and observe significant reduction in charge densities over time

10.2 String Breaking vs Mass

We can also see similar suppression of string breaking as well as mass is increased.

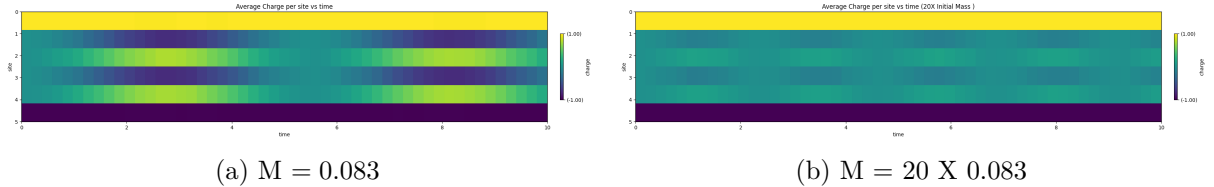


Figure 10: Comparison of average charge for low and high mass regime starting from initial charges at the ends. As for all other simulations $M_{initial} = 0.083$ and $g = 1.29$. For figure (b) we use $20.M_{initial}$ and observe significant reduction in charge densities over time. Trotter steps = 50

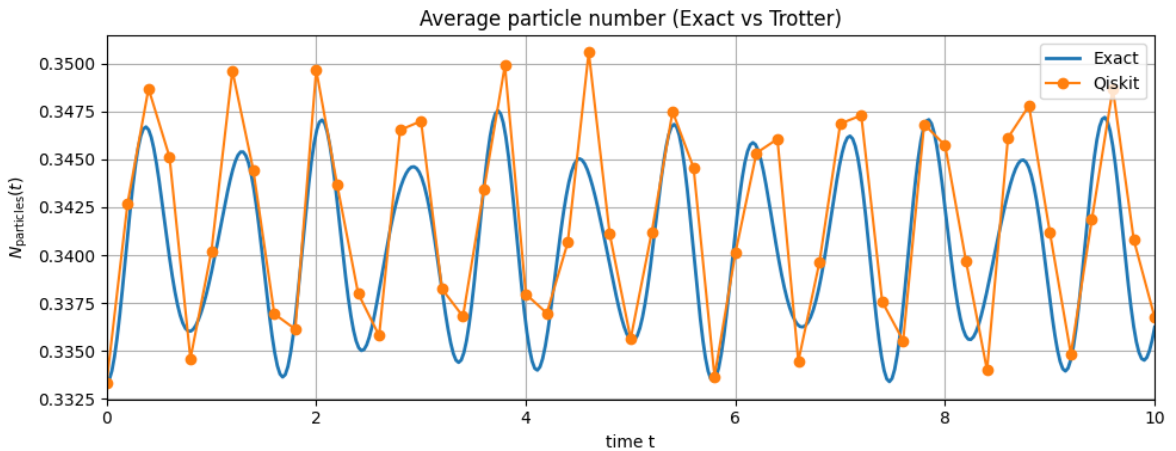


Figure 11: $N_{sites} = 6$. Comparison of average Particle number between 50 trotter steps vs exact evolution for high mass regime in case of string breaking. We see that the values hover around $2/6$ which denote no new particles are being formed other than those in the initial state

11 Dynamical Phase Transition and the θ -Vacuum

In the previous sections, we analyzed the Schwinger model with a vanishing topological angle ($\theta = 0$). In this regime, the vacuum $|1010\dots\rangle$ is stable and separated from excited states by a

mass gap. However, the full richness of the model emerges when we consider the effect of the θ -angle, which acts as a background electric field.

At $\theta = \pi$, the physics becomes critical. The effective background field creates a competition between the bare vacuum and a state filled with particle-antiparticle pairs. In the thermodynamic limit, this results in a phase transition where the chiral condensate $\Sigma = \langle \bar{\psi} \psi \rangle$ flips sign.

11.1 Dynamical Sweep Protocol

To observe this transition on the quantum computer without re-deriving the entire Hamiltonian for non-zero θ , we employ a dynamical mapping. The effect of the θ -angle can be absorbed into the mass and hopping terms via a chiral rotation. We simulate the transition by making the Hamiltonian parameters time-dependent over a period $t \in [0, 1]$:

$$m(t) = M \cos(2\pi t). \quad (26)$$

By evolving the system from $t = 0$ to $t = 1$, we effectively sweep the topological angle θ from 0 to 2π . The critical point $\theta = \pi$ corresponds to $t = 0.5$, where the effective mass term flips sign.

11.2 Results: The Chiral Condensate

We initialized the system in the heavy-mass vacuum ($N = 8$) and performed a second-order Trotterized evolution under this time-dependent Hamiltonian. We measured the chiral condensate $\Sigma(t) \propto \sum_n (-1)^n \langle Z_n \rangle$ at each time step. The results are shown in Figure 12.

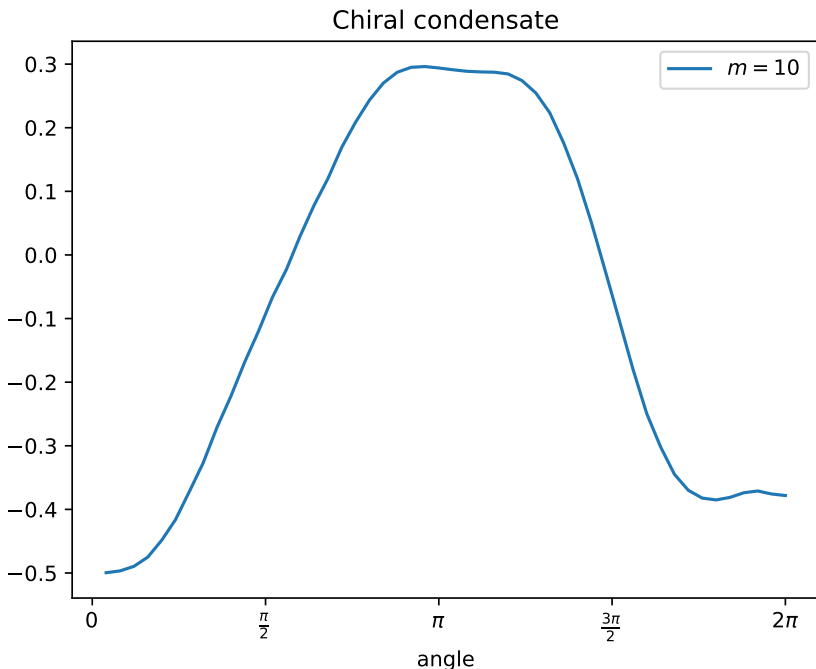


Figure 12: Dynamical sweep of the Chiral Condensate for an $N = 8$ lattice. The x-axis represents the accumulated phase angle $\theta = 2\pi t$. The system starts in the trivial vacuum ($\Sigma \approx -0.5$). As the sweep approaches $\theta = \pi$, the order parameter flips sign, indicating a restructuring of the vacuum. The transition is smooth rather than discontinuous due to the finite lattice size ($N = 8$) and the finite rate of the sweep, which smoothes out the first-order transition into a crossover.

This experiment demonstrates the capability of the quantum processor to simulate not just static properties, but also complex dynamical phase structures.

References

- [1] Nhung H. Nguyen, Minh C. Tran, Yingyue Zhu, Alaina M. Green, C. Huerta Alderete, Zohreh Davoudi, and Norbert M. Linke. Digital quantum simulation of the schwinger model and symmetry protection with trapped ions. *PRX Quantum*, 3(2), May 2022.
- [2] Zohreh Davoudi. Tasi/cern/kitp lecture notes on "toward quantum computing gauge theories of nature", 2025.
- [3] John Kogut and Leonard Susskind. Hamiltonian formulation of wilson's lattice gauge theories. *Phys. Rev. D*, 11:395–408, Jan 1975.
- [4] David Tong. Lectures on gauge theory. <https://www.damtp.cam.ac.uk/user/tong/gaugetheory.html>, 2018. Lecture notes, University of Cambridge.